Journal of Infrared, Millimeter, and Terahertz Waves (2025) 46:13
https://doi.org/10.1007/s10762-024-01031-7

RESEARCH

Implementation Methods for Transmission Zeros in Groove Gap Waveguide Filters at W-Band

Daniel Miek[1] · Patrick Boe[1] · Fynn Kamrath[1] · Michael Höft[1]

Received: 30 August 2024 / Accepted: 24 December 2024 / Published online: 11 January 2025

Abstract

In this paper, three groove gap waveguide (GGW) filters are presented, which utilize different techniques to create transmission zeros (TZs) in the W-band. First, a fourth-order filter with cross-coupling of non-adjacent cavities realizes five TZs. The filter is implemented using a stacked cavity approach, which simplifies the realization of cross-couplings with positive and negative signs. The source to load cross-coupling realizes one TZ more than predicted from theory. In the second filter, two off-centered posts with partial height are used to realize two TZs. These posts act as strongly frequency-dependent coupling elements and enable the realization of TZs in an inline filter topology. An interdigital-pin implementation has been used since otherwise, the distance between the posts and the sidewalls is too small to allow manufacturing using the Computerized Numerical Control (CNC) milling approach. The third filter is of fourth order and implements two TZs by using a stub-loaded cavity approach. All filters are designed as a proof of concept in the W-band (75–110 GHz) to verify the manufacturability at high-frequency bands. The manufactured components are realized by high-precision CNC milling and measurement results show good agreement with the simulation for all proposed filters.

Keywords Frequency-dependent coupling · Groove Gap Waveguide (GGW) · Interdigital-pin · Source to load cross-coupling · Stub-loaded cavity · W-band filter

✉ Daniel Miek
dami@tf.uni-kiel.de

Patrick Boe
pabo@tf.uni-kiel.de

Fynn Kamrath
flk@tf.uni-kiel.de

Michael Höft
mh@tf.uni-kiel.de

[1] Chair of Microwave Engineering, Kiel University, Kaiserstr. 2, Kiel 24143, Germany

1 Introduction

The use of transmission zeros (TZs) in the transfer function of a generalized Chebyshev filter response is a well-established strategy to improve the near-band rejection properties of a filter by maintaining the filter order, which corresponds to the number of resonances [1, 2]. This is especially important since the quality factor of a resonator decreases at high center frequencies and hence the insertion loss of a filter increases. Therefore, in many cases, it is desirable to keep the filter order as low as possible.

In waveguide techniques, several strategies are known to introduce TZs, as for example, the cross-coupling of cavities [3, 4], the use of stubs [5, 6], the extracted pole technique [7], bypass couplings [8] and frequency-dependent couplings [9, 10]. Considering different manufacturing strategies, the TZ implementing mechanisms can be applied up to the WR-1 band [11].

Recently, the groove gap waveguide (GGW) technology was used for the design and manufacturing of microwave components [12–14]. In comparison to conventional waveguide devices, the sidewall of the waveguide channel is formed by at least two rows of periodically arranged pins [14]. As an important advantage, the pins do not require any contact to the cover of the component. While the manufacturing of several pin rows might be interpreted as a disadvantage due to the higher effort, it is an advantage that there is a small gap between the pins and the cover. Therefore, no losses due to contact resistances can occur as it is the case considering conventional waveguide components manufactured with an H-plane cut. If the pin structure is designed properly, wave propagation in the desired frequency band is not possible and avoids leakage from the waveguide channel, which is formed by the pins.

While in many publications a prototype for validation is manufactured by milling, other manufacturing techniques can be utilized as well. In Santiago et al. [15] selective laser melting as an additive manufacturing method was used for fabrication whereas in Santiago et al. [16] stereolithography is applied for manufacturing. At higher frequency bands, micromachining techniques [17, 18] or the screen printing technique as recently shown in [19, 20] can be used for the realization of GGW filters. Disadvantageously, all and especially both latter manufacturing techniques are not as widespread as CNC milling machines for the fabrication of microwave components.

Considering the development of GGW filters in the literature, two main restrictions become obvious:

- In many cases, all-pole filters without any TZs are proposed and realized as proof of concept, as it is, e.g., shown in [12, 14, 21–26].
- Many filters were realized in the lower gigahertz-regime (below W-band), e.g., [12, 14, 21–27].

This paper therefore demonstrates the design and realization of three GGW filters having two and five TZs. The filters are fabricated using CNC milling and are designed in the W-band (75–110 GHz) in order to validate, that the designs are suitable for manufacturing at these high frequencies. First, the TZs are realized by the use of a stacked filter topology using cross-couplings between non-adjacent resonators, second by using frequency-dependent coupling apertures, realized as partial height posts, and third by utilizing a stub-loaded cavity approach.

This paper is organized as follows: Section 2 discusses the pin structures used for the design and fabrication of the prototypes. In Section 3, the design and realization of the stacked cavity filter approach is shown. Sections 4 and 5 discuss similar aspects for a GGW filter with frequency-dependent couplings and a GGW filter with stubs, respectively. Section 6 provides a comparison between the results presented here and other filters from the literature. Finally, Section 7 draws a conclusion.

2 Groove Gap Waveguide Approach

The GGW technique was introduced in Kildal et al. [13]. Since then, various modifications and variations have been discussed, including, e.g., the ridge groove gap waveguide approach [22] or the half-height pin approach [28]. For the filter realizations discussed in this paper, mainly two different pin patterns are used. The filters proposed in Sections 3 and 5 use a conventional pin pattern, where all pins are located on the same ground plate. This configuration is denoted here as combline-pin arrangement. The pin structure is shown in Fig. 1a. The pins have a height of $h_{pin,1} = 1.1\,\text{mm}$, a side length of $w_{pin,1} = 0.4\,\text{mm}$ and a periodical distance between each other of $p_1 = 0.8\,\text{mm}$, leading to a gap of 0.4 mm between adjacent pins. The dispersion diagram reveals, that modes can propagate in the periodic pin structure either below the W-band or at the upper edge (107 GHz) of the W-band, which is far away from the filter center frequency. All simulations of this and the following chapters are carried out using CST microwave studio.

Figure 1b shows the pin structure as used for the second filter discussed in Section 4. Here, in contrast to the first pattern, an interdigital-pin arrangement as recently discussed in [29, 30] is used. The pins are therefore located on the ground plate (gray pins in Fig. 1b) as well as on the cover (red pins in Fig. 1b). From the manufacturing point of view, the interdigital-pin arrangement has the advantage, that in the final assembly, pins can be placed closer to each other without changing the cutter diameter

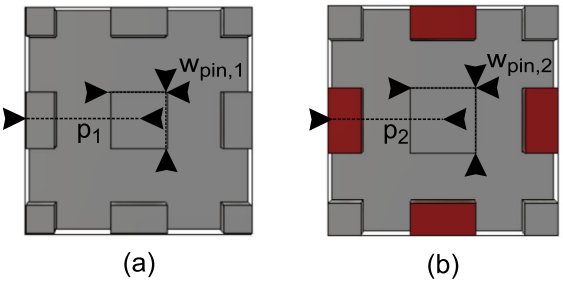

Fig. 1 Pin structure of **a** combline-pin arrangement and **b** interdigital-pin arrangement. The dimensions are as follows: $w_{pin,1} = 0.4$ mm, $p_1 = 0.8$ mm (0.4 mm gap between pins), $w_{pin,2} = 0.4$ mm, and $p_2 = 0.7$ mm (0.3 mm gap between pins)

in the CNC manufacturing process. In the case of the second filter presented here, the posts with partial height (which introduce the TZs) must be located very close to the sidewall, where manufacturing would be nearly impossible using the classical milling approach in combination with a combline-pin arrangement. The dimensions of the second pin structure are slightly different compared to the first one. The pins have a height of $h_{pin,2} = 1.2\,\text{mm}$, a side length of $w_{pin,2} = w_{pin,1} = 0.4\,\text{mm}$ and a periodical distance between each other of $p_2 = 0.7\,\text{mm}$. The dispersion diagram reveals, that the whole W-band is free from modes in the periodic pin structure.

3 Groove Gap Waveguide Filter with Stacked Topology

3.1 Synthesis and Design

The filter proposed in this section uses a stacked cavity approach, similar as in waveguide techniques [31, 32]. Stacked cavity constructions were also proposed in GGW technology, but at lower frequency bands [21, 33, 34].

The filter investigated here is designed to achieve a return loss level of at least $RL = 20\,\text{dB}$ between the band edges located at $f_1 = 86\,\text{GHz}$ and $f_2 = 87\,\text{GHz}$. Four resonators in a stacked cavity approach are used to realize the filter response. The filter set-up is shown in Fig. 2a–c and is similar to the set-up in, e.g., Miek et al. [35]. Cavities one and two are located in the top layer, while cavities three and four are located in the bottom layer. The coupling within the individual layers takes place using inductive coupling irises (black marked in Fig. 2b and c). The coupling between both layers is realized using a thin sheet of metal, in which coupling holes are drilled. The coupling hole between cavities two and three is placed at the sidewall, implementing a dominant magnetic coupling. In contrast, cavities one and four are cross-coupled by an iris placed in the cavity center, enabling a dominant electric field cross-coupling. With this cross-coupling, two symmetrically placed TZs are introduced to the filter response [1]. The diameter of the cross-coupling hole determines the position of the TZs.

In order to further increase the number of TZs, a source to load cross-coupling is added to the filter. In a stacked cavity configuration, it is very easy to add this coupling, which can be seen as a general advantage. The source to load cross-coupling is characterized by the distance l_0 and by the diameter d_{SL} (see Fig. 2). The coupling topology associated with the filter set-up and used for the initial filter design is shown in Fig. 2d. The corresponding coupling matrix for TZ positions at $f_{TZ,LP} = \{\pm j5.3 \pm j2\}$ and a return loss of $RL = 20\,\text{dB}$ is shown in Table 1. The filter main path is realized by dominant magnetic field couplings, which might be counted positively with respect to the coupling matrix approach. The cross-coupling between cavities one and four is then counted negative due to the electric field coupling. To realize at least four TZs, the source to load cross-coupling should be realized as a dominant magnetic field coupling. This could, e.g., be enabled by placing a coupling hole on both sides of the source/load port. However, in previous studies (e.g., [35, 36]) it results that a single coupling hole in the center of the waveguide channel has a superior performance with respect to the number and flexibility of the introduced TZs. This behavior is obtained

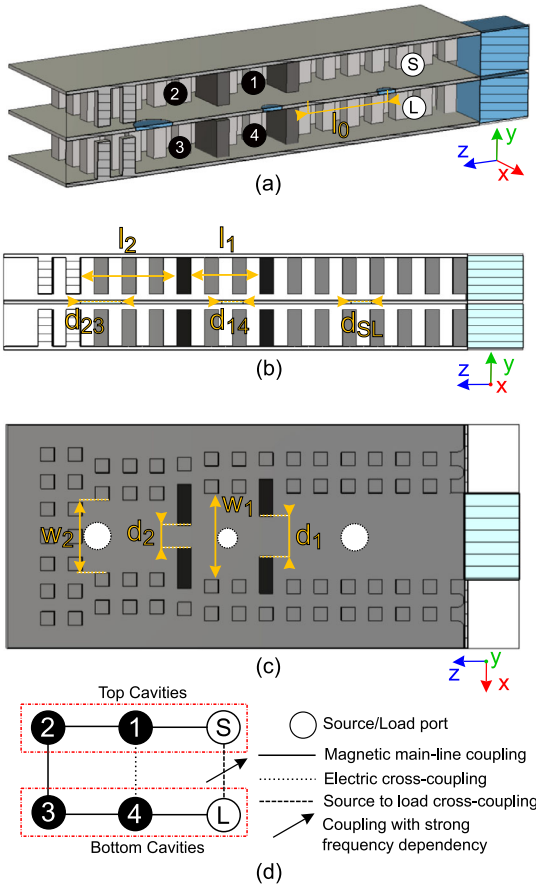

Fig. 2 GGW filter in stacked topology: **a** perspective view (cut along *y*-*z* plane), **b** side view, and **c** top view on bottom or cover layer (the position of the coupling holes is indicated). The dimensions are as follows (all in mm): $l_0 = 2.525$, $l_1 = 2$, $l_2 = 2.8$, $d_1 = 1.173$, $d_2 = 0.638$, $w_1 = 2.522$, $w_2 = 2.132$, $d_{SL} = 0.58$, $d_{14} = 0.62$, and $d_{23} = 1.18$. The top and bottom layers have identical dimensions. **d** coupling diagram used for filter synthesis

due to the dispersive characteristic of the source to load cross-coupling, which is marked with an arrow in the corresponding coupling scheme.

The whole set-up is realized using two pin rows as sidewalls. While cavities one/four are formed by using two pins along the z-axis (along cavity length l_1), cavities two/three consist of three pins (along cavity length l_2). Considering Fig. 1, the length of the cavities is therefore $l_1 = 2\,\text{mm}$ and $l_2 = 2.8\,\text{mm}$. The tuning of the center frequency is enabled by varying the widths w_1 and w_2. The couplings within one layer are realized as conventional inductive irises and are tuned by their width d_1 and d_2. As the filter is symmetrical regarding the *x*-*z* plane, the top and bottom layers have identical dimensions.

The filter design and tuning process might follow conventional rules based on coupling matrix extraction and tuning techniques, while Table 1 is used for initial

Table 1 Coupling matrix description of stacked GGW filter

–	S	1	2	3	4	L
S	0	1.022	0	0	0	0.006
1	1.022	0	0.868	0	−0.186	0
2	0	0.868	0	0.738	0	0
3	0	0	0.738	0	0.868	0
4	0	−0.186	0.0	0.868	0	1.022
L	0.006	0	0	0	1.022	0

synthesis. Four transmission zeros should be realized by the set-up from the theory point of view, two of which are below and two above the passband [37].

After tuning/optimizing the filter to the desired return loss level within the prescribed band-edges, it has in total five TZs on the normalized frequency axis at the following positions: $f_{TZ,LP} = \{-j5.17, -j1.615, j2.59, j5.485, j7.58\}$. On the one hand, it is worth mentioning that the TZs are asymmetric despite the symmetric filter set-up, which results from dispersion effects within the filter and the source to load cross-coupling. A discussion on this topic takes place in Section 3.2.

This behavior can exemplary be examined by a simulation model, which consists only of the source/load port, the source to load cross-coupling as well as a detuned first/last resonator (see Fig. 3). The latter ones are included in the simulation model to account for loading effects. As a result from the S-parameters, TZs occur even in the absence of a filter set-up. The introduced fifth TZs is therefore a result of the dispersive behavior of the source to load cross-coupling.

For further investigations, Fig. 4 shows the result of a corresponding parameter study. There, the frequency of all available TZs in the frequency range between 80 and 95 GHz is shown in dependency from the parameter l_0. In this case, the whole filter including the source to load cross-coupling is simulated. Four TZs are expected by the set-up to be present. As can be seen in Fig. 4, the frequency of the lowest TZ (red marked) decreases by increasing l_0. Otherwise, a fifth TZ appears (green marked) and can be placed near the passband. If l_0 is chosen too large, the TZs represented by the

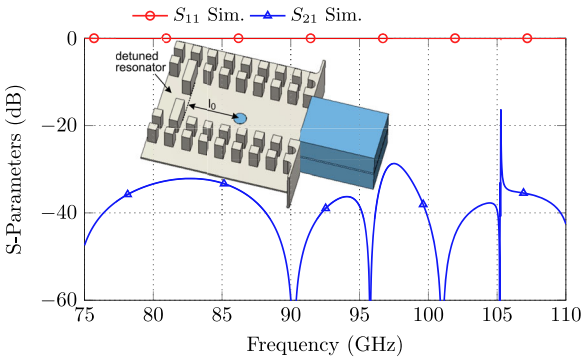

Fig. 3 Simulated S-parameters of the set-up in the inset. The simulation model includes the source and load ports, the source to load cross-coupling ($l_0 = 2.525$ mm), inductive irises to the first/last resonator as well as a detuned first/last resonator

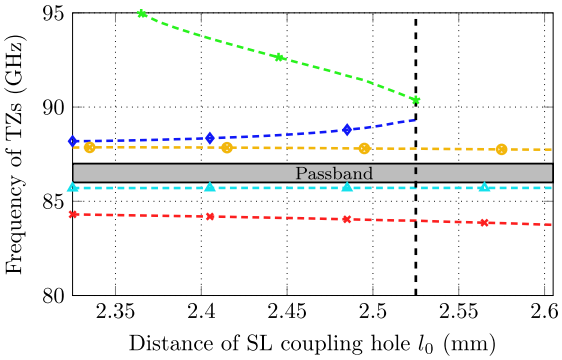

Fig. 4 Position of all TZs between 80 and 95 GHz in dependency from parameter l_0. The vertical dashed line visualizes the value of l_0 used in the manufactured prototype

blue and green curve merge with each other and only one TZ (ocher marked) remains above the passband. Other suitable values for l_0 or even d_{SL} than the one presented here might be found as well.

On the other hand, the fifth TZ at normalized frequency $j7.58$ is introduced by the source to load cross-coupling as well. The TZ arises due to the strongly dispersive behavior of the source to load cross-coupling [38, 39].

3.2 Frequency-Dependent Coupling Matrix Description

The initial coupling matrix used for filter design as shown in Table 1 generates a symmetric filter response as no diagonal cross-couplings M_{24} and M_{1L} are included in the coupling scheme. However, the simulation results as well as the study in Fig. 4 show a clearly asymmetric filter response without having diagonal cross-couplings included in the filter layout. Three circumstances are identified to create the asymmetry in the filter response:

- The SL cross-coupling creates one additional (one more than expected) TZ above the passband, leading to an inherent asymmetric filter response. The influence of the position of the SL cross-coupling on the frequency of all other TZs is discussed in Fig. 4.
- The SL cross-coupling itself is strongly dispersive as can be seen by the S-parameters in Fig. 3.
- The inductive irises realizing the mainline couplings show a frequency-dependent behavior as well. This is especially valid for the inductive irises which couple the cavities located on the same layer.

The frequency dependency of these couplings might be included in an extended coupling matrix description, where all mainline couplings as well as the SL coupling show a frequency dependency. Two assumptions have been made:

- The SL cross-coupling can be described by a second-order polynomial in the frequency range near the passband. The frequency-dependent coupling factor can be calculated from the simulated S-parameters generated by the sub-structure in Fig. 3 and evaluated by, e.g., Ding et al. [1] Eq. 8.48.

Table 2 Frequency-dependent coupling matrix description of the stacked GGW filter

–	S	1	2	3	4	L
S	0	$1.02 + 0.001\omega$	0	0	0	$M_{SL}(\omega)$
1	$1.02 + 0.001\omega$	0.2	$0.87 + 0.13\omega$	0	-0.21	0
2	0	$0.87 + 0.13\omega$	0.08	$0.78 - \omega$5.56e-5	0	0
3	0	0	$0.78 - \omega$5.56e-5	0.08	$0.87 + 0.13\omega$	0
4	0	-0.21	0.0	$0.87 + 0.13\omega$	0.2	$1.02 + 0.001\omega$
L	$M_{SL}(\omega)$	0	0	0	$1.02 + 0.001\omega$	0

The entry $M_{SL}(\omega)$ is defined in Eq. 1

- The filter is symmetric regarding the x-z plane. Hence, the frequency dependency of the couplings lying above each other must be identical.

The final description in terms of a frequency-dependent coupling matrix is given in Table 2 and is obtained by using an optimization algorithm in Matlab.

$$M_{SL}(\omega) = 0.009 - 3.37 \cdot 10^{-4}\omega - 5.498 \cdot 10^{-5}\omega^2 \tag{1}$$

Figure 5 shows a comparison between the simulation results and the frequency-dependent coupling matrix description from Table 2. Obviously, the coupling matrix fits the simulated S-parameters quite well in the near passband frequency range.

3.3 Manufacturing and Measurement Results

The filter is realized consisting of three parts. The manufacturing cut is along the x-z-axis (compare Fig. 2). Both parts of the housing are separated by a thin metal foil with a thickness of 0.1 mm. Figure 6 shows a photograph of the disassembled filter. The input and output ports are realized as conventional waveguide ports and are bent by 90° to enable access to the measurement ports.

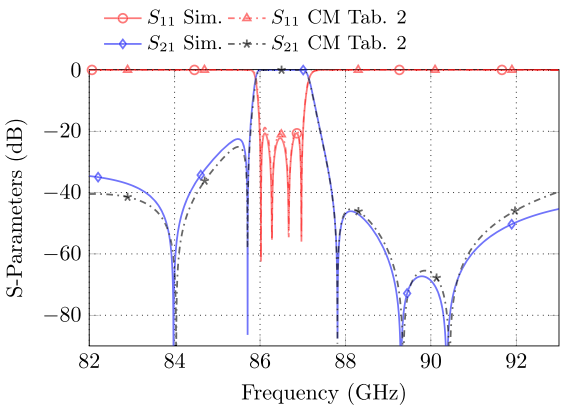

Fig. 5 Comparison of the simulated S-parameters and the S-parameters generated by the coupling matrix in Table 2

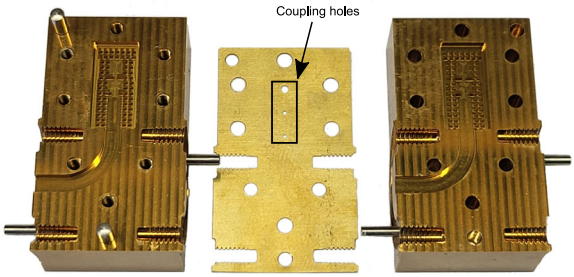

Fig. 6 Photograph of stacked cavity filter manufactured from brass. Left and right: bottom and cover, respectively. Center: 0.1 mm thick brass foil which is placed between bottom and cover

The measurement results in comparison to the simulation are shown in Fig. 7. Two TZs below the passband and three TZs above the passband are realized by the set-up. The TZ at 90.3 GHz arises due to the dispersive characteristic of the source to load cross-coupling. The peak at approx. 98.5 GHz emerges due to resonances of the coupling irises.

The measured filter has a return loss of at least 16.5 dB, while the insertion loss in the passband center is approx. 2.05 dB. From this measurement, an unloaded Q-factor of $Q_u \approx 670$ can be derived.

4 GGW Filter with Frequency-Dependent Couplings

4.1 Synthesis and Design

Another approach for the flexible realization of TZs is the use of frequency-dependent coupling apertures such as posts with partial height. Posts with partial height were introduced in waveguide filter design in bandpass and bandstop filters [10, 40, 41]. In the high-frequency regime always the limitation arises, that the post must be located very close to the waveguide sidewall, which makes manufacturing with CNC milling

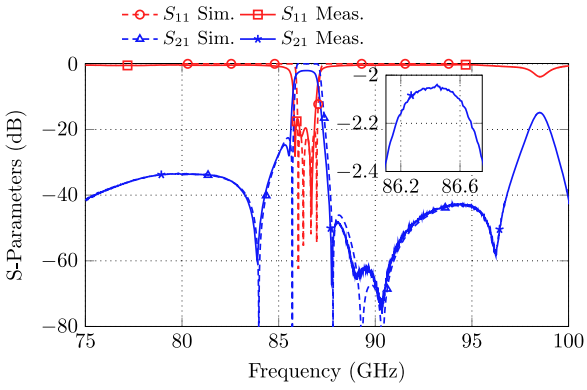

Fig. 7 Measurement results in comparison to the simulation for the stacked cavity filter

machines difficult or impossible. The interdigital-pin GGW approach as used here is a simple technique to avoid these difficulties. The proof-of-concept filters were manufactured using a CNC milling machine capable of using a minimum cutter diameter of 0.3 mm.

The feasibility is proven in this paper by integrating two posts with partial height in the filter design at W-band. For the design of the proposed filter the pin structure in Fig. 1b is used. This is required because the distance between the posts which realize the waveguide sidewall and the post with partial height is very small. The distance mainly influences the coupling strength between adjacent cavities while the height is mainly used to control the position of the TZ introduced by the post. Hence, by using the interdigital-pin approach as discussed in Fig. 1b, a small distance to the adjacent pin can be realized by a manageable manufacturing effort.

The filter proposed here is of third order and realizes two TZs above the passband. Figure 8a shows the 3-D model of the filter. Note, that gray colored pins are located on the ground plate and red colored pins are located on the cover, which is not shown in the figure. The source and load ports are coupled by inductive irises to the first and third cavities, respectively. The second cavity is coupled to the first as well as to the third cavity by a post with partial height. Similar as in the filter of the former section, the length of the individual cavities l_i is kept constant at 2.4 mm, while the center frequency of each resonator is adjusted by the cavity width w_i. The filter design process can be accomplished by first designing a third-order filter without any TZs and only consisting of inductive irises as coupling elements. After matching this filter, the coupling aperture between cavities one and two as well as between cavities two and three can be replaced

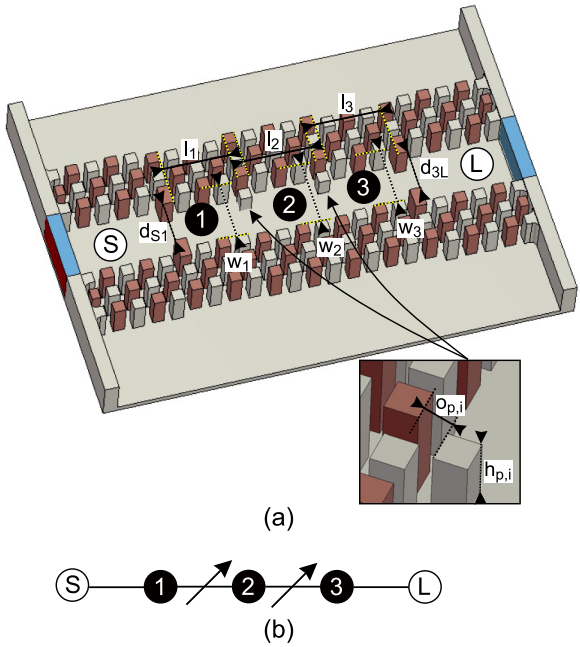

Fig. 8 Interdigital-pin groove gap waveguide filter with frequency-dependent couplings. **a** Filter set-up (pins on the ground plate are colored gray, pins located on the cover are colored red). The cover is not shown. The dimensions are as follows (all in mm): $d_{S1} = 1.502$, $d_{3L} = 1.508$, $l_1 = l_2 = l_3 = 2.4$, $w_1 = 2.136$, $w_2 = 2.401$, $w_3 = 2.134$, $h_{p,1} = h_{p,2} = 0.727$, $o_{p,1} = o_{p,2} = 0.179$. **b** Coupling matrix topology with coefficients as in Table 3

Table 3 Coupling matrix description of the third-order filter with two frequency-dependent couplings (compare Fig. 8b)

–	S	1	2	3	L
S	0	1.042	0	0	0
1	1.042	−0.61	−1.04+0.37ω	0	0
2	0	−1.04+0.37ω	−0.61	−1.01+0.26ω	0
3	0	00	−1.01+0.26ω	−0.38	1.09
L	0	0	0	1.09	0

by a post with partial height. The footprint of both posts is chosen identical to those forming the GGW channel. The only degrees of freedom are therefore given by the height $h_{p,i}$ as well as by the distance from the sidewall $o_{p,i}$. The dimensions might be found using parameter sweeps/optimization or coupling matrix extraction and tuning techniques. A suitable coupling matrix description, which is obtained by optimization, is given in Table 3 [41, 42]. Note, that the frequency dependency of the posts with partial height is accounted for by a frequency-dependent coupling matrix entry at positions M_{12} and M_{23}.

The coupling matrix corresponds to the specifications of a return loss level of $RL = 21\,\text{dB}$ between the band edges located at $f_1 = 84.5\,\text{GHz}$ and $f_2 = 86\,\text{GHz}$ ($B = 1.5\,\text{GHz}$, $f_0 \approx 85.25\,\text{GHz}$, $FBW = 1.76\%$). The TZs above the passband are located at the normalized frequencies $f_{TZ,LP,1} = j2.74$ and $f_{TZ,LP,2} = j3.92$.

The corresponding filter topology is shown in Fig. 8b, where couplings marked with an arrow denote a frequency-dependent coupling. These are realized by the posts with partial height.

All final dimensions are given in the capture of Fig. 8. It is worth mentioning that the distance between the posts with partial height and the pins, which realize the sidewall, is too small for manufacturing using a combline-pin arrangement ($o_{p,1} = o_{p,2} = 0.179\,\text{mm}$).

The flexibility of the approach is exemplary demonstrated in Fig. 9, where simulated S-parameter results with different TZ patterns are realized. Table 4 gives an overview

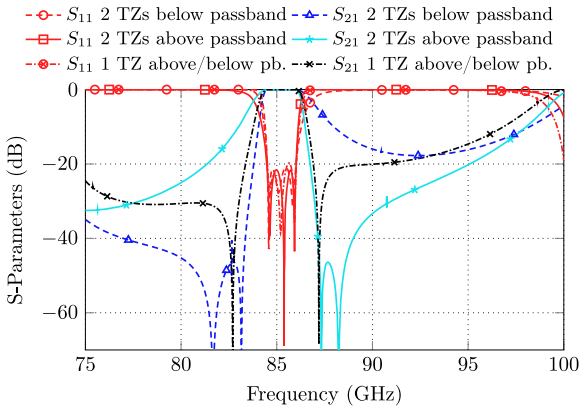

Fig. 9 Different TZ configurations of the filter set-up in Fig. 8a. The curve with both TZs above the passband is obtained by using the dimensions of the caption in Fig. 8

Table 4 Dimensions of posts with partial height for the simulated S-parameter responses in Fig. 9 (all in mm)

–	Both TZs above passband	Both TZs below passband	One TZ above and one below passband
$o_{p,1}$	0.179	0.083	0.07
$o_{p,2}$	0.179	0.081	0.092
$h_{p,1}$	0.727	0.942	0.858
$h_{p,2}$	0.727	0.942	0.901

of the used dimensions. Beyond the case where both TZs are above the passband, it is likewise possible to place both TZs below the passband or one TZ above and one below the passband. Note, that not only the dimensions of the posts must be adapted but other filter dimensions as well.

4.2 Manufacturing and Measurement Results

The filter was manufactured twice using the materials brass and aluminum. Figure 10 shows a picture of the filter manufactured from brass. As can be seen from the picture, the manufacturing effort increases as both filter halves require high-precision manufacturing since both parts contain pins. Furthermore, a high-precision alignment between both components is critically required. As otherwise already mentioned, a combline-pin arrangement is not possible using CNC milling manufacturing due to the small distance between the sidewall pins and the posts with partial height.

The measurement results of both filters in comparison to the simulation are shown in Fig. 11. Manufacturing or alignment tolerances for the filter manufactured from brass lead to a detuned filter response. As one TZ is shifted to higher frequencies, a manufacturing error of one of the posts with partial height seems to be the most probable reason. Therefore, Section 4.3 provides a tolerance investigation in order to give statements on the required manufacturing accuracy. Otherwise, the S-parameter response of the filter manufactured from aluminum is nearly coincident with the simulated S-parameters, which means that the required manufacturing accuracy can be achieved by modern high-precision CNC milling machines. From this measurement

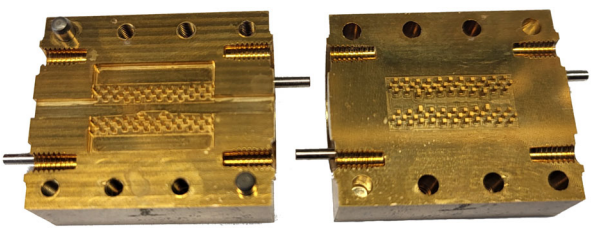

Fig. 10 Photograph of the filter with two partial height posts manufactured from brass. Due to the interdigital-pin approach, both components contain a pin structure. Left: Bottom part. Right: Cover

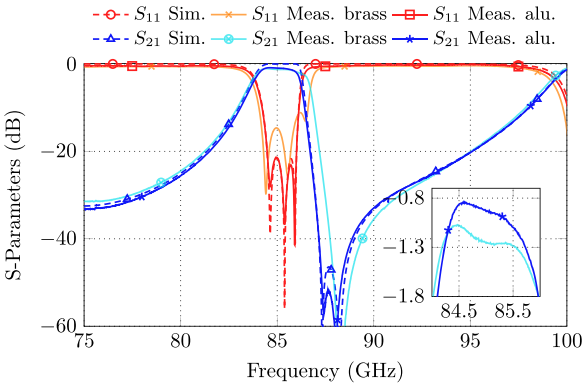

Fig. 11 Measurement results in comparison to the simulation for filters manufactured from brass and aluminum

an unloaded quality factor of $Q_{u,alu} \approx 610$ can be obtained, while a return loss level of 21 dB is achieved. For the filter manufactured from brass a lower unloaded quality factor of $Q_{u,brass} \approx 440$ is obtained.

4.3 Tolerance Investigation

The measurement results in Fig. 11 motivate the implementation of a tolerance investigation with respect to the most sensitive elements, which are the posts with partial height. Figure 12 shows the resulting S-parameters if the first or second post with partial height are reduced or increased in their height by 10 µm from the ideal value as defined in Fig. 8. A similar study is done in Fig. 13, where the offset position of the posts with partial height is varied in positive and negative direction by 10 µm. This value is chosen as it might be seen as a benchmark for filter manufacturing with respect to milling. The remaining parameters maintain their ideal values. Two results are noticeable:

- Reducing the offset $o_{p,i}$ compared to the ideal dimension leads to an increased bandwidth while an increase of the offset leads to a reduced bandwidth. However,

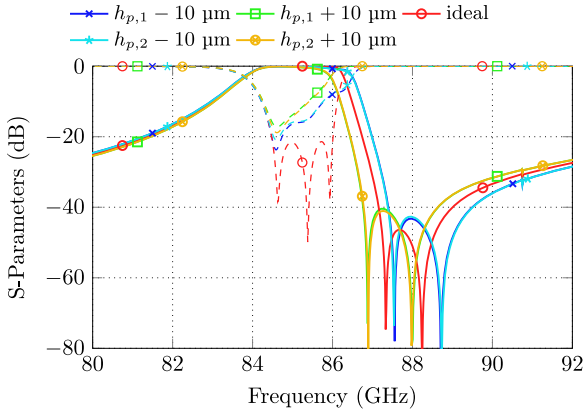

Fig. 12 Simulated S-parameters if the height $h_{p,i}$ of the first or second post with partial height is increased or decreased by 10 µm

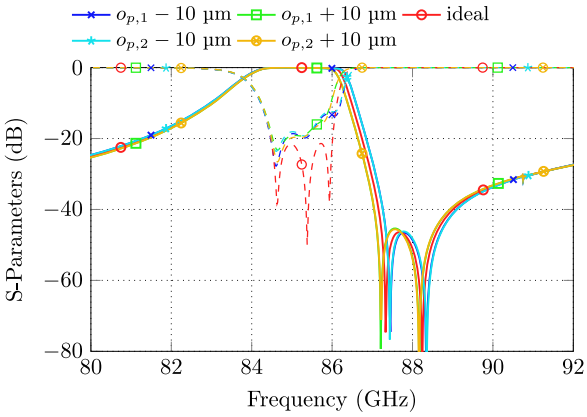

Fig. 13 Simulated S-parameters if the offset from the sidewall $o_{p,i}$ of the first or second post with partial height is increased or decreased by 10 µm

the increase or decrease in bandwidth detunes the filter response. Furthermore, the maximum achievable bandwidth is limited by the distance between the partial height post and the sidewall. The TZ positions are minor affected.

- A variation of the height $h_{p,i}$ by the same amount distorts the filter performance more drastically. The TZs are shifted to a lower frequency by increasing the height while they are shifted to a higher frequency if the height is decreased.

As a result, for the manufacturing of these types of filter milling machines with a nominal tolerance smaller than 10 µm should be used. Apart from the milling itself, the use of high-precision alignment pins is absolutely necessary as well.

5 Stub-loaded GGW Filter

5.1 Synthesis and Design

The last approach for the integration of TZs in the filter response of a GGW filter proposed in this paper is based on using stubs. Stub-loaded waveguide filters are, e.g., discussed in [5, 43]. An approach combining the microstrip GGW technique and stub-loaded ring resonant modes was recently proposed in Shi et al. [44].

A second-order building block is shown in Fig. 14. It is realized using the same pin pattern as shown in Fig. 1a, while a pin height of 1.2 mm is used. The building block consists of an input and output port, which are coupled by inductive irises to the GGW base cavity. On top of this cavity, a stub is placed to be manufactured in the lid. The stub is characterized by a width of w_s, a height of h_s, a length of l_s and might has an offset from the center position denoted as o_c. The base cavity has a fixed length of $l_c = 2.8$ mm, as it is realized by three rows of pins with a constant distance from each other. The center frequency is adapted using the width of the cavity w_c. It is worth to note that the input and output coupling apertures are realized by interdigital-pins, which are red marked in Fig. 14. These pins are therefore connected to the cover. As in the case of the former filter configuration, these pins can be positioned closer to

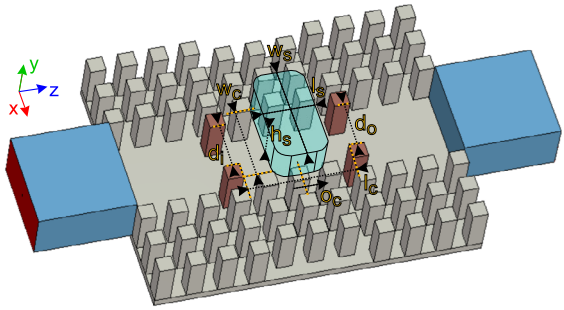

Fig. 14 Second-order building block consisting of a main cavity and a stub

the pins which form the sidewall without the need for a smaller cutter diameter in the manufacturing process.

An exemplary S-parameter response of this building block with weak excitation is shown in Fig. 15. As one can see, two resonances and one TZ appear. The associated electric field distribution at the resonance frequencies is shown in Fig. 16. The electric field in (a) corresponds to the reflection zero at 86.97 GHz and can be associated with a TM-mode resonance in the stub. The electric field configuration in (b) is otherwise similar to a TE_{101}-mode in a waveguide cavity and corresponds to the reflection zero at 89.87 GHz.

The building block can be tuned to realize a second-order filter with the TZ either below or above the passband. The position of the TZ is mainly influenced by parameters w_c and h_s [43]. Both S-parameter responses with associated dimensions are shown in Fig. 17. The dimensions are tuned to realize the band edges at frequencies $f_1 = 86.41\,\text{GHz}$ and $f_2 = 87.19\,\text{GHz}$ ($B = 780\,\text{MHz}$, $f_0 \approx 86.8\,\text{GHz}$, $FBW = 0.9\%$).

A fourth (or even higher) order filter can be obtained by coupling several of these building blocks by inductive irises. The proposed filter set-up is shown in Fig. 18a. Two cavities are realized on the base plate having a length of l_{c1} and l_{c2} and a width of w_{c1} and w_{c2}, respectively. The cavities are coupled to the source and load port

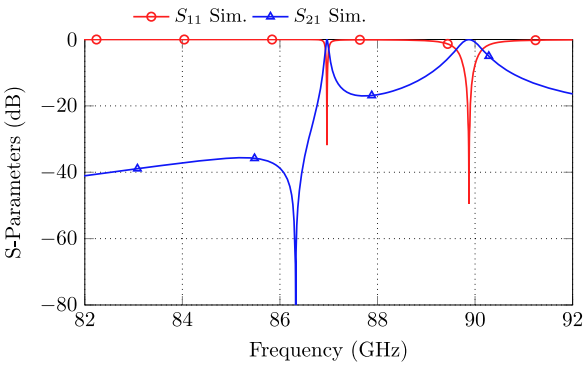

Fig. 15 S-parameter response of the configuration in Fig. 14 with parameters as follows (all in mm): $d_i = d_o = 1.2$, $l_c = 2.8$, $w_c = 1.9$, $h_s = 0.856$, $w_s = 2.52$, $l_s = 1.349$, $o_c = 0$

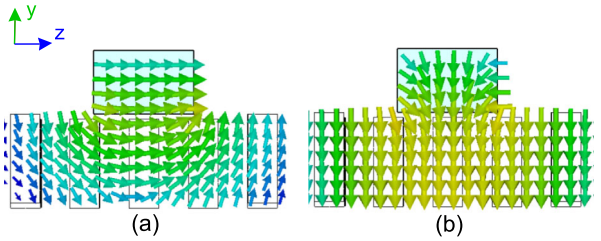

Fig. 16 Electric field configuration of the resonances in the S-parameter response in Fig. 15 at **a** 86.97 GHz and **b** 89.87 GHz

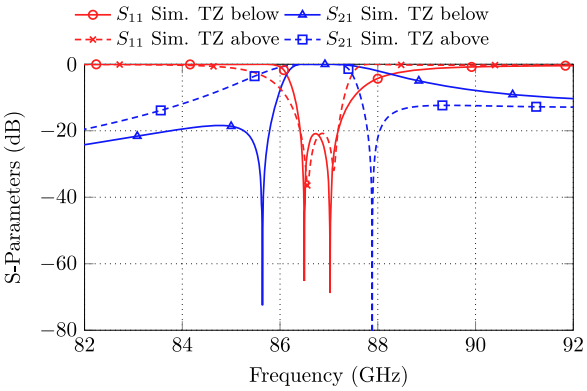

Fig. 17 S-parameter responses of the second-order filter from Fig. 14 with parameters as follows (all in mm). TZ below passband: $d_i = d_o = 1.446$, $w_c = 1.9$, $h_s = 0.856$, $l_s = 1.349$, $w_s = 2.52$, $o_c = 0$. TZ above passband: $d_i = d_o = 1.446$, $w_c = 1.935$, $h_s = 0.867$, $l_s = 0.7$, $w_s = 2.52$, $o_c = 0$. In both configurations the stub has a radius of 0.35 mm

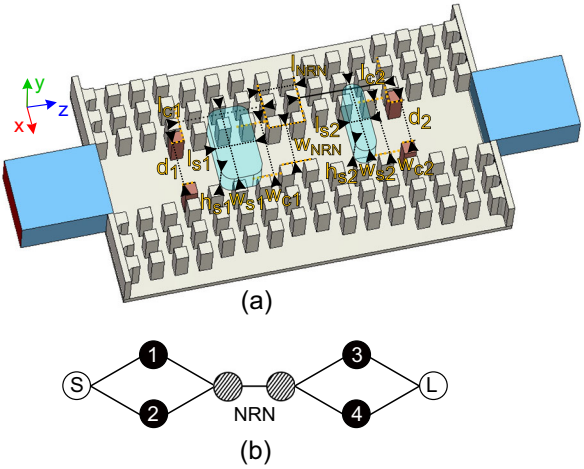

Fig. 18 **a** Fourth-order stub-loaded GGW filter. Pins connected to the cover are marked in red. The stubs are located in the cover and are marked as transparent blue. The dimensions are as follows (all in mm): $d_1 = 1.5, d_2 = 1.5, l_{c1} = 2.8, w_{c1} = 1.902, l_{c2} = 2.8, w_{c2} = 1.936, l_{s1} = 1.349, l_{s2} = 0.7, h_{s1} = 0.856$, $h_{s2} = 0.883$, $w_{s1} = 2.516$, $w_{s2} = 2.452$, $w_{NRN} = 1.375$, $l_{NRN} = 1.2$. The second stub has an offset in z-direction from the cavity center of 0.12 mm while the first stub has no offset. **b** Associated coupling topology

by inductive irises with diameter d_1 and d_2. The associated posts are marked in red and are connected to the cover plate. Both cavities are loaded with a TM-mode stub with length l_{s1} and l_{s2}, width of w_{s1} and w_{s2} as well as height h_{s1} and h_{s2}. The stub-loaded cavities are coupled with each other using a long and wide-opened inductive iris with parameters l_{NRN} and w_{NRN}. Due to the long aperture, these irises might been interpreted as two consecutive non-resonating nodes (NRNs) in the coupling scheme (compare Fig. 18) [43, 45].

In the design process, both stub-loaded cavities might be designed independently from each other. By coupling them together, S-parameters suitable for optimization are obtained after conducting a parameter sweep for w_{NRN} and choosing the most appropriate value. Note, that l_{NRN} is not varied in this design due to the fixed ground plane of the pins and the fixed distance between them. The filter is then optimized for a desired bandwidth, whereby the specified center frequency should already be defined when designing the second-order building blocks. As design goals for the fourth-order filter the band edges are placed at $f_1 = 86.1\,\text{GHz}$ and $f_2 = 87.7\,\text{GHz}$ ($B = 1.6\,\text{GHz}$, $f_0 \approx 86.9\,\text{GHz}$, $FBW = 1.84\%$). The filter matching takes place by optimization. The simulation time can be decreased by, e.g., exploiting the y-z symmetry plane. A comparison between the S-parameters prior and after optimization is shown in Fig. 19.

After optimization, the dimensions as shown in the caption of Fig. 18 are obtained. They are used for fabricating the prototype as discussed in Section 5.2.

5.2 Manufacturing and Measurement Results

The filter shown in Fig. 18 was manufactured as proof of concept. For manufacturing aluminum was chosen. The manufactured filter is shown in Fig. 20. As both components contain structures that contribute to the S-parameter response, a high-precision alignment is required. Note, that the cover on the right-hand side of Fig. 20 not only contains both stubs but also the interdigital-pins of the input and output coupling (compare red-marked pins in Fig. 18).

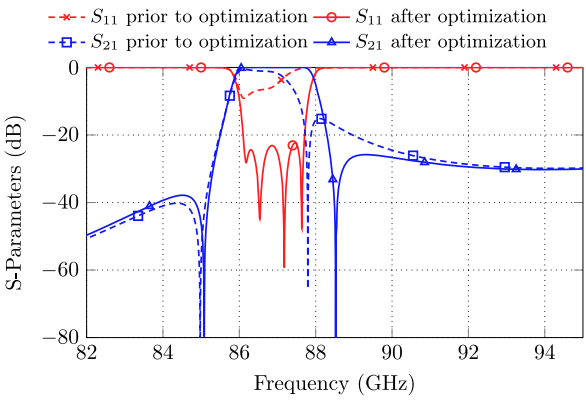

Fig. 19 S-parameters of the filter set-up in Fig. 18 directly after cascading two second-order building blocks (prior to optimization) as well as after optimization to the desired specifications

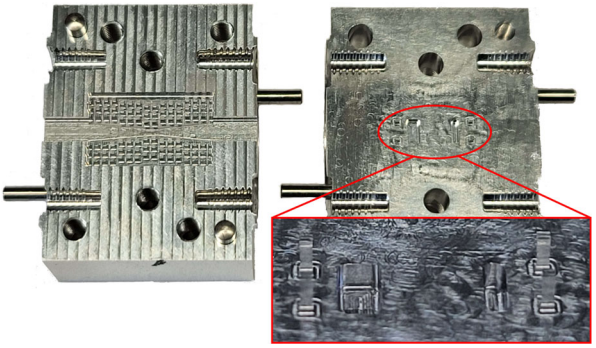

Fig. 20 Photograph of the fourth-order stub-loaded GGW filter manufactured from aluminum. Left: Base structure, right: lid containing both stubs and posts for input/output coupling

The measurement results in comparison to the simulation are shown in Fig. 21. The filter is matched to a return loss of 11 dB while the insertion loss is around 1.05 dB at the passband center, leading to an unloaded Q-factor of $Q_u \approx 860$.

The manufacturing of the base cavities is not associated with any difficulties compared to both filters of the former sections. The most reasonable source for increased tolerances might be the interdigital-pins used for realizing the input and output coupling. These pins lead to the need for extremely precise manufacturing at a height including the interdigital-pins and both stubs, which makes the design prone to errors.

An alternative approach is shown in the inset of Fig. 22, which shows a similar model as in Fig. 18a. However, the input and output couplings are realized as conventional inductive irises, which further eases manufacturing using CNC milling machines. In this case, only both stubs are manufactured in the lid but no pin structures. The corresponding simulated S-parameters are shown in Fig. 22 as well.

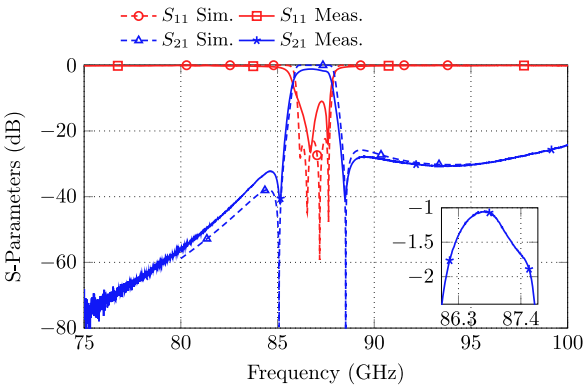

Fig. 21 Measurement results of the stub-loaded GGW filter in comparison to simulation

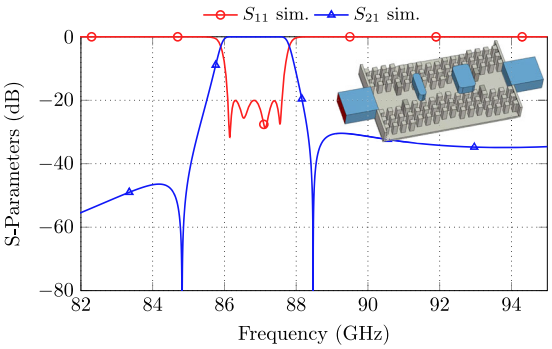

Fig. 22 Simulated S-parameters of a similar set-up as shown in Fig. 18, where the input and output couplings are realized as conventional inductive irises

6 Comparison

Table 5 shows a comparison of the filters discussed in this paper (denoted as filter 1 to filter 3) with other filters published in the literature. As can be seen, the filters discussed here reveal good insertion loss and return loss performance at the W-band waveguide standard. As discussed in the introduction, many filters are designed without incorporating TZs in the filter response and at lower frequency bands.

7 Conclusion

In this paper, three different approaches for the realization of TZs in groove gap waveguide filters are described. In the first filter, destructive interference between non-adjacent cavities as a very conventional approach for the realization of TZs is used. As proof of concept, a stacked filter is designed and manufactured. In the second filter posts with partial height, which act as strongly dispersive coupling apertures, are used to introduce two TZs. Finally, an approach using stub-loaded groove gap waveguide cavities is employed. All filters are manufactured using the well-established CNC

Table 5 Comparison of the filters in this work with other GGW filters

Manufact. techn.	Waveguide standard	Order	TZs	f_c (GHz)	FBW	IL (dB)	RL (dB)	Ref
CNC	V-band	5	0	≈ 60.5	2.5%	≈ 1.5	> 13	[12]
CNC	V-band	5	0	59.7	1.34%	≈ 1.7	> 9	[26]
CNC	Q-band	4	0	≈ 39.5	2.5%	≈ 1.1	> 19	[24]
CNC	Ka-band	3	0	35	1%	≈ 1	> 13	[21]
CNC	V-band	5	0	60.2	2.49%	≈ 1.5	> 13	[23]
CNC	Ka-band	7	0	≈ 37.37	1.5%	≈ 1.5	> 17	[22]
CNC	E-band	4	2	73.5	8% (3-dB)	≈ 0.45	> 10	[34]
3-D printing	W-band	5	0	94	3.19%	≈ 0.45	> 15	[16]
CNC	W-band	4	5	≈ 86.5	1.16%	≈ 2.05	> 16.5	filter 1
CNC	W-band	3	2	≈ 85.25	1.76%	≈ 0.85	> 21	filter 2
CNC	W-band	4	2	≈ 86.8	0.9%	≈ 1.05	> 11	filter 3

milling technique and proof the feasibility of the proposed approaches in the W-band. A comparison of the achieved results with the literature is provided.

Author Contributions Conceptualization, D.M., P.B., F.K., and M.H.; methodology, D.M., P.B., F.K., and M.H.; formal analysis and investigation, D.M., P.B., F.K., and M.H.; writing—original draft preparation, D.M.; writing—review and editing, P.B., F.K., and M.H.; supervision, M.H.; all authors have read and agreed to the published version of the manuscript.

Funding Open Access funding enabled and organized by Projekt DEAL.

Data Availability All data generated or analyzed during this study is included in this article.

Declarations

Ethical Approval Not applicable

Consent to Participate The authors consent to participate.

Consent for Publication The authors consent to publish.

Competing Interests The authors declare no competing interests.

References

1. R. J. Cameron, C. M. Kudsia, and R. R. Mansour, *Microwave Filters for Communication Systems*. Wiley, 2007.
2. J.-S. Hong, *Microstrip Filters for RF/Microwave Applications*. John Wiley & Sons Inc., 2011.
3. J.-Q. Ding, S.-C. Shi, K. Zhou, D. Liu, and W. Wu, "Analysis of 220-GHz low-loss quasi-elliptic waveguide bandpass filter," *IEEE Microwave and Wireless Components Letters*, vol. 27, no. 7, pp. 648–650, Jul. 2017.
4. J. Ding, D. Liu, S. Shi, and W. Wu, "W-band quasi-elliptical waveguide filter with cross-coupling and source-load coupling," *Electronics Letters*, vol. 52, no. 23, pp. 1960–1961, Nov. 2016.
5. S. Bastioli and R. V. Snyder, "Stubbed waveguide cavity filters," *IEEE Transactions on Microwave Theory and Techniques*, vol. 67, no. 12, pp. 5049–5060, Dec. 2019.
6. J. Bornemann and J. Uher, "H-plane waveguide filters with E-plane dispersive inverters for high-power applications," in *2004 10th International Symposium on Antenna Technology and Applied Electromagnetics and URSI Conference (Ottawa, ON, Canada)*. IEEE, Jul. 2004, pp. 1–4.
7. J. Montejo-Garai, J. A. Ruiz-Cruz, J. M. Rebollar, M. J. Padilla-Cruz, A. Onoro-Navarro, and I. Hidalgo-Carpintero, "Synthesis and design of in-line N-order filters with N real transmission zeros by means of extracted poles implemented in low-cost rectangular H-plane waveguide," *IEEE Transactions on Microwave Theory and Techniques*, vol. 53, no. 5, pp. 1636–1642, May 2005.
8. S. Amari and U. Rosenberg, "Characteristics of cross (bypass) coupling through higher/lower order mode and their applications in elliptic filter design," *IEEE Transactions on Microwave Theory and Techniques*, vol. 53, no. 10, pp. 3135–3141, Oct. 2005.

9. P. Kozakowski, A. Lamecki, M. Mongiardo, M. Mrozowski, and C. Tomassoni, "Computer-aided design of in-line resonator filters with multiple elliptical apertures," in *2004 IEEE MTT-S International Microwave Symposium Digest (IEEE Cat. No.04CH37535) (IMS, Fort Worth, TX, USA)*. IEEE, Jun. 2004, pp. 611–614.
10. M. Politi and A. Fossati, "Direct coupled waveguide filters with generalized chebyshev response by resonating coupling structures," *40th European Microwave Conference (EuMC, Paris, France)*, pp. 966–969, Sep. 2010.
11. S. Liu, J. Hu, Z. Xuan, Y. Zhang, and R. Xu, "Micromachined WR-1.0 waveguide band-pass filter," in *IEEE International Conference on Microwave and Millimeter Wave Technology (ICMMT, Beijing, China)*. IEEE, Jun. 2016, pp. 1–3.
12. A. Berenguer, M. Baquero-Escudero, D. Sanchez-Escuderos, B. Bernardo-Clemente, and V. E. Boria-Esbert, "Low insertion loss 61 GHz narrow-band filter implemented with groove gap waveguides," in *2014 44th European Microwave Conference (Rome, Italy)*. IEEE, Oct. 2014, pp. 191–194.
13. P.-S. Kildal, E. Alfonso, A. Valero-Nogueira, and E. Rajo-Iglesias, "Local metamaterial-based waveguides in gaps between parallel metal plates," *IEEE Antennas and Wireless Propagation Letters*, vol. 8, pp. 84–87, Dec. 2009.
14. A. U. Zaman, P. Kildal, and A. A. Kishk, "Narrow-band microwave filter using high-Q groove gap waveguide resonators with manufacturing flexibility and no sidewalls," *IEEE Transactions on Components, Packaging and Manufacturing Technology*, vol. 2, no. 11, pp. 1882–1889, Nov. 2012.
15. D. Santiago, M. A. G. Laso, T. Lopetegi, and I. Arregui, "Novel design method for millimeter-wave gap waveguide low-pass filters using advanced manufacturing techniques," *IEEE Access*, vol. 11, pp. 89 711–89 719, Aug. 2023.
16. D. Santiago, A. Tamayo-Domínguez, M. A. G. Laso, T. Lopetegi, J.-M. Fernández-González, R. Martínez, and I. Arregui, "Robust design of 3D-printed W-band bandpass filters using gap waveguide technology," *Journal of Infrared, Millimeter, and Terahertz Waves*, vol. 44, no. 1-2, pp. 98–109, Dec. 2022.
17. S. Rahiminejad, H. Raza, A. U. Zaman, S. Haasl, P. Enoksson, and P. S. Kildal, "Micromachined gap waveguides for 100 GHz applications," in *2013 7th European Conference on Antennas and Propagation (EuCAP, Gothenburg, Sweden)*. IEEE, Apr. 2013, pp. 1935–1938.
18. Y. Shi, J. Zhang, M. Zhou, W. Feng, B. Cao, and W. Che, "Miniaturized W-band gap waveguide bandpass filter using the MEMS technique for both waveguide and surface mounted packaging," *IEEE Transactions on Circuits and Systems II: Express Briefs*, vol. 66, no. 6, pp. 938–942, Jun. 2019.
19. K. Reuter, P. Boe, D. Miek, M. Höft, T. Studnitzky, C. Zhong, T. Weißgärber, and I. O. Leon, "3-D screen printing: Efficient additive manufacturing of groove gap waveguide filters in D-band," *IEEE Microwave and Wireless Technology Letters*, vol. 34, no. 6, pp. 721–724, Jun. 2024.
20. P. Boe, K. Reuter, D. Miek, T. Studnitzky, C. Zhong, T. Weissgaerber, and M. Höft, "High-precision additive manufacturing of groove gap waveguide filters in D-band," in *Accpeted for Publication at 2024 Asia-Pacific Microwave Conference (APMC, Bali, Indonesia)*. IEEE, Nov. 2024.
21. B. Ahmadi and A. Banai, "Direct coupled resonator filters realized by gap waveguide technology," *IEEE Transactions on Microwave Theory and Techniques*, vol. 63, no. 10, pp. 3445–3452, Oct. 2015.
22. E. A. Alos, A. U. Zaman, and P. Kildal, "Ka-band gap waveguide coupled-resonator filter for radio link diplexer application," *IEEE Transactions on Components, Packaging and Manufacturing Technology*, vol. 3, no. 5, pp. 870–879, May 2013.
23. A. Berenguer, D. Sánchez-Escuderos, B. Bernardo-Clemente, M. Baquero-Escudero, and V. Boria, "Groove gap waveguide as an alternative to rectangular waveguide for H-plane components," *Electronics Letters*, vol. 52, no. 11, pp. 939–941, May 2016.
24. A. del Olmo-Olmeda, M. Baquero-Escudero, V. E. Boria-Esbert, A. Valero-Nogueira, and A. J. Berenguer-Verdu, "A novel band-pass filter topology for millimeter-wave applications based on the groove gap waveguide," in *2013 IEEE MTT-S International Microwave Symposium Digest (MTT, Seattle, WA, USA)*. IEEE, Jun. 2013, pp. 1–4.
25. M. Rezaee and A. Zaman, "Capacitive-coupled groove gap waveguide filter," in *12th European Conference on Antennas and Propagation (EuCAP, London, UK)*. Institution of Engineering and Technology, Apr. 2018, pp. 1–5.
26. M. Rezaee, A. U. Zaman, and P.-S. Kildal, "A groove gap waveguide iris filter for V-band application," in *2015 23rd Iranian Conference on Electrical Engineering (Tehran, Iran)*. IEEE, May 2015, pp. 462–465.

27. M. Rezaee and A. U. Zaman, "Groove gap waveguide filter based on horizontally polarized resonators for V-band applications," *IEEE Transactions on Microwave Theory and Techniques*, vol. 68, no. 7, pp. 2601–2609, Jul. 2020.
28. F. Fan, J. Yang, and P.-S. Kildal, "Half-height pins - a new pin form in gap waveguide for easy manufacturing," in *2016 10th European Conference on Antennas and Propagation (EuCAP, Davos, Switzerland)*. IEEE, Apr. 2016.
29. D. Sun, X. Chen, J.-Y. Deng, L.-X. Guo, W. Cui, K. Yin, Z. Chen, C. Yao, and F. Huang, "Gap waveguide with interdigital-pin bed of nails for high-frequency applications," *IEEE Transactions on Microwave Theory and Techniques*, vol. 67, no. 7, pp. 2640–2648, Jul. 2019.
30. D. Miek, F. Kamrath, P. Boe, K. Braasch, and M. Höft, "Interdigital-pin groove gap W-band waveguide filter," in *2022 24th International Microwave and Radar Conference (MIKON, Gdansk, Poland)*. IEEE, Sep. 2022.
31. J. Kocbach and K. Folgerø, "Design procedure for waveguide filters with cross-couplings," in *2002 IEEE MTT-S International Microwave Symposium Digest (Cat. No.02CH37278) (IMS, Seattle, WA, USA)*. IEEE, Jun. 2002, pp. 1449–1452.
32. E. Ofli, "Analysis and design of microwave and millimeter-wave filters and diplexer," phdthesis, Swiss Federal Institute of Zurich, 2004.
33. H. S. Farahan and W. Bösch, "Ku-band gap waveguide filter with negative coupling structure," *2019 European Microwave Conference in Central Europe (EuMCE, Prague, Czech Republic)*, pp. 290–293, May 2019.
34. T. Xiu, Y. Yao, H. Jiang, X. Cheng, C. Wang, B. Wang, J. Yu, and X. Chen, "Design of a compact and low-loss E-band filter based on multilayer groove gap waveguide," *IEEE Microwave and Wireless Components Letters*, vol. 31, no. 11, pp. 1211–1214, Nov. 2021.
35. D. Miek, A. Reinhardt, F. Daschner, and M. Höft, "Improved fully canonical W-band waveguide filter," *IEEE MTT-S International Microwave Symposium (IMS, Philadelphia, PA, USA)*, pp. 1245–1248, Jun. 2018.
36. D. Miek, A. Morán-López, J. A. Ruiz-Cruz, and M. Höft, "Improved fully canonical phase equalized W-band waveguide filter with dispersive coupling inverter," in *2018 48th European Microwave Conference (EuMC, Madrid, Spain)*. IEEE, Sep. 2018, pp. 166–169.
37. R. J. Cameron, "Advanced coupling matrix synthesis techniques for microwave filters," *IEEE Transactions on Microwave Theory and Techniques*, vol. 51, no. 1, pp. 1–10, Jan. 2003.
38. D. Miek, K. Braasch, C. Bartlett, F. Kamrath, P. Boe, and M. Höft, "Coupling matrix description of WR-3 waveguide filter with multiple transmission zeros created by source to load cross-coupling," in *2022 14th German Microwace Conference (GeMiC, Ulm, Germany)*. IEEE, May 2022, pp. 17–20.
39. D. Miek, K. Braasch, F. Kamrath, P. Boe, and M. Höft, "Compact WR-3 filter with improved rejection properties by double source-load cross-coupling," in *2024 15th German Microwave Conference (GeMiC, Duisburg, Germany)*. IEEE, Mar. 2024.
40. U. Rosenberg and S. Amari, "A novel band-reject element for pseudoelliptic bandstop filters," *IEEE Transactions on Microwave Theory and Techniques*, vol. 55, no. 4, pp. 742–746, Apr. 2007.
41. L. Szydlowski, A. Lamecki, and M. Mrozowski, "Coupled-resonator waveguide filter in quadruplet topology with frequency-dependent coupling – a design based on coupling matrix," *IEEE Microwave and Wireless Components Letters*, vol. 22, no. 11, pp. 553–555, Nov. 2012.
42. L. Szydlowski, A. Lamecki, and M. Mrozowski, "Coupled-resonator filters with frequency-dependent couplings: Coupling matrix synthesis," *IEEE Microwave and Wireless Components Letters*, vol. 22, no. 6, pp. 312–314, Jun. 2012.
43. D. Miek, F. Kamrath, K. Braasch, P. Boe, and M. Höft, "Quasi-elliptical stub-based multi-resonance waveguide filters with low manufacturing complexity for mm-wave applications," *IEEE Journal of Microwaves*, vol. 3, no. 1, pp. 70–83, Jan. 2023.
44. Z.-H. Shi, F. Wei, L. Yang, and R. Gómez-García, "High-selectivity inverted microstrip gap waveguide bandpass filter using hybrid cavity and stub-loaded ring resonant modes," *IEEE Transactions on Circuits and Systems II: Express Briefs*, vol. 71, no. 1, pp. 146–150, Jan. 2024.
45. S. Amari and U. Rosenberg, "New building blocks for modular design of elliptic and self-equalized filters," *IEEE Transactions on Microwave Theory and Techniques*, vol. 52, no. 2, pp. 721–736, feb 2004.